High energy storage performance of (1-x)Ba$_{0.9}$Ca$_{0.1}$TiO$_3$-xBaSn$_{0.1}$Ti$_{0.9}$O$_3$ bulk ceramics

Shichang Han[a], **Lingling Cui**[b,*], **Zhiwei Li**[c], **Kuo Luan**[a]

[a] College of Mechanical Engineering, Wanjiang University of Technology, Ma'anshan 243031 China
[b] School of Mechanical Engineering, Nantong Institute of Technology, Nantong 226002 China
[c] School of Automotive Engineering, Nantong Institute of Technology, Nantong 226002 China

*Corresponding author, e-mail: cuilingling2024@163.com

ABSTRACT: Despite their efficiency in energy storage, lead-based materials present substantial environmental and health hazards due to their toxicity. Improper disposal of lead can lead to lead contamination of water and soil, endangering both humans and wildlife. Furthermore, the extraction and processing of lead exacerbate environmental degradation. Consequently, the transition to lead-free alternatives is essential for mitigating these impacts and enhancing the sustainability and safety of energy storage technologies. In this study, lead-free (1-x)Ba$_{0.9}$Ca$_{0.1}$TiO$_3$-xBaSn$_{0.1}$Ti$_{0.9}$O$_3$ (1-x)BCT-xBST, x = 0–0.12 ceramics were fabricated using the traditional solid-state method. The effects of BST doping on the energy storage properties of BCT ceramics were systematically investigated. Scanning electron microscopy (SEM) revealed a trend of diminishing average grain size in the ceramics as the value of x increased. X-ray diffraction (XRD) and Raman scattering analyses confirmed the coexistence of tetragonal and orthorhombic phases, particularly at x = 0.10. Notably, the (1-x)BCT-xBST ceramics exhibited a high dielectric constant, low dielectric loss, large recoverable energy density (W = 138 mJ/cm^3), and an impressive energy storage efficiency (η = 87.51%) under a low electric field of 30 kV/cm. In summary, the (1-x)BCT-xBST ceramics significantly advance eco-friendly energy storage, combining high performance with environmental sustainability.

KEYWORDS: BaTiO$_3$, lead-free ceramics, energy storage properties, dielectric properties

INTRODUCTION

Energy storage ceramics have become a focal point of interest in the field of capacitor technology due to their exceptional properties, including high dielectric permittivity, negligible hysteresis losses, and impressive electric breakdown strength [1–3]. Among these materials, lead-based ceramics, particularly lead zirconate titanates (PbZr$_{1-x}$Ti$_x$O$_3$, PZT), have historically been the preferred choice for energy storage applications due to their ability to achieve high energy densities, with records as high as 558.1 J/cm^3 at 2805 kV/cm [4–7]. However, the environmental and health hazards associated with lead oxide have necessitated the urgent development of lead-free alternatives [8].

In response to this need, the (1-x)Ba$_{0.9}$Ca$_{0.1}$TiO$_3$-xBaSn$_{0.1}$Ti$_{0.9}$O$_3$ (1-x)BCT-xBST system has surfaced as a viable candidate for lead-free electro-ceramics, boasting a significant piezoelectric constant of 600 pC/N [9]. Within the realm of ABO$_3$ perovskite structures, the superior piezoelectric characteristics are frequently linked to the morphotropic phase boundary (MPB) region, where phase transitions such as those from tetragonal to orthorhombic are observed in BCT and BST [10]. The energy storage capabilities of BCT-BST ceramics have been the subject of recent studies for potential use in capacitors, with energy densities reported at 1.41 J/cm^3 for BCT and 0.37 J/cm^3 for BST under electric fields of 150 kV/cm

and 190 kV/cm, respectively [11, 12]. Furthermore, the (1-x)BaTiO$_3$-xCaSnO$_3$ ceramics demonstrated an energy density of 1.57 J/cm^3 at 230 kV/cm [13].

Despite the extensive research on high electric field regions for maximizing energy density [14], this strategy has raised safety concerns [15], particularly for applications in wearable and flexible electronic systems where lower electric fields are essential for safe and effective energy storage [16–18]. This has led to a paradigm shift in the research community, with a growing emphasis on understanding the implications of low electric fields on capacitor energy density. Recent studies have documented energy densities of 30 mJ/cm^3 for Ba(Ti,Sn)O$_3$ and 164 mJ/cm^3 for 0.5BCT-0.5BZT ceramics at 10 kV/cm and 40 kV/cm, respectively [19, 20]. These findings have laid the groundwork for a new direction in energy storage research.

In this work, lead-free (1-x)Ba$_{0.9}$Ca$_{0.1}$TiO$_3$-xBaSn$_{0.1}$Ti$_{0.9}$O$_3$ (1-x)BCT-xBST, x = 0–0.12 ceramics were fabricated using the traditional solid-state method. The effects of BST doping on various aspects of BCT ceramics, including their energy storage properties, dielectric constants, phase structure and microstructure, were systematically studied. The results demonstrate that the (1-x)BCT-xBST ceramics exhibit enhanced energy storage capabilities at low electric fields and offer a promising pathway for developing safe and efficient energy storage solutions in emerging electronic applications.

MATERIALS AND METHODS

The (1-x)BCT-xBST (x = 0–0.12) ceramics were fabricated using $BaCO_3$ (99.9%), $CaCO_3$ (99.9%), TiO_2 (99.9%), and SnO_2 (99.5%) as starting materials. Stoichiometric powders of the BCT-xBST system were mixed for 4 h in ethanol medium, then dried and calcined at 1200 °C for 4 h in air. The BCT-xBST powders were mixed with 8 wt% polyvinyl alcohol (PVA) binder solution, pressed into disks, and sintered at 1480 °C for 2 h.

Phase structure of the (1-x)BCT-xBST ceramics was characterized via an X-ray diffraction system (XRD, Rigaku D/max-2500/PC, Cu $K\alpha_1$, λ=1.5406 Å, Japan). The Raman spectroscopy was tested by a Raman microscope (Raman, InVia, Renishaw, UK) at 100–1000 cm^{-1}. The sintered ceramics were observed after being thermally etched at 1150 °C for 2 h using a scanning electron microscope (SEM, HITACHI S-4300). The Wincell and Winplote software calculated the samples unit cell volumes. The densities of the ceramics were measured using the Archimedes method. The sintered pellets were polished on both sides to obtain parallel surfaces; then, silver paste was fired at 650 °C for 30 min as electrodes. Dielectric properties of the sintering ceramics were characterized by the precision impedance analyzer (4294 Agilent Inc., Malaysia). Polarization-electric field (P-E) hysteresis loops of ceramics were measured using a Radiant Precision Premier LC ferroelectric material test system (Radiant Technologies Inc., USA).

RESULTS AND DISCUSSION

Fig. 1A shows XRD patterns of the (1-x)BCT-xBST ceramics with different x content. The diffraction peaks were standardized according to the JCPDS file no: PDF#81-2203. All samples presented a single perovskite-type structure, indicating that BST had diffused into the $BaTiO_3$ lattice and formed a complete solid solution in the discussed composition. In addition, the samples showed a tetragonal phase observed by splitting the (200)/(002) peaks with x = 0–0.02 at around 2θ∼45° (Fig. 1B). The diffraction peak of the ceramics at x = 0.04–0.12 was fitted by the full diffraction profile fitting of the MDI Jade 5.0 software to characterize the phase evolution further, as shown in Fig. 1C. The (200) peak could be fitted to $(002)_T$, $(200)_T$ and $(002)_O$ peaks at x = 0.04, showing a growing tendency to merge into a single peak at x = 0.10. The result suggested the coexistence of the orthorhombic phase and the tetragonal phase at the composition range between 0.04 to 0.10. The diffraction peaks shifted to lower angles with increasing x values, corresponding to the cell volume expansion. The introduction of BST, the Rietveld analysis of the resultant XRD patterns based on the space group of tetragonal (T) phase and orthorhombic (O) were shown in Fig. 1D,E, and the results were presented in Table 1. The fitting

parameter χ^2 values of the samples were all below 8, which proved the validity of Rietveld analysis. Based on the parameters, the phase comprised the dominant O phase with 83.11% and the T phase with 16.89% at x = 0. The content of the O phase kept decreasing until reaching 7.44% at x = 0.12, accompanied by the increase of the T phase content to 92.56%. The generation of permanent electric dipoles in the T phase stimulated the emergence of polar nanodomains, resulting in superior relaxation properties. The lattice parameter refinement program further measured the variation of lattice parameters c/a and cell volume, as shown in Fig. 2A. The lattice parameters (c/a) and the cell volume increased gradually with increasing x values. Hence, it could be deduced that Sn^{4+} (0.71 Å) might enter into Ti^{4+} (0.68 Å) [10].

Raman spectra with excellent sensitivity in probing the structural information are a better means to characterize the structures evolution further [19, 20]. Fig. 2B exhibits the Raman spectra of the (1-x)BCT-xBST ($0 \leqslant x \leqslant 0.12$) ceramics in the frequency range of 100–1000 cm^{-1} at room temperature. The Raman spectra of the ceramics were similar to that of $BaTiO_3$, suggesting that these compositions shared the basic unit structure [21]. The six broad modes at 150, 217, 270, 306, 518, and 717 cm^{-1} with $0 \leqslant x \leqslant 0.10$ at room temperatures signified the tetragonal $BaTiO_3$ [19]. The strengthening of the bands near 306 cm^{-1} corresponded to vibrations of Ti-O bonds [22], which could be attributed to the diffusion of BST into the $BaTiO_3$ lattice in the discussed composition. The dip at around 150 cm^{-1} weakened gradually with x = 0–0.10, indicating that the long-range ferroelectric order was destroyed, accompanied by the phase transition process from the tetragonal phase to the orthorhombic phase [20].

Fig. 3 shows the SEM images of the (1-x)BCT-xBST ceramics at x = 0–0.12. The microstructures of the samples were greatly improved to be uniformly distributed and fully densified with increasing x values. The inset of each micrograph in Fig. 4 shows the average grain size of individual A–G compositions being 56.6 μm, 41.7 μm, 32.6 μm, 24.2 μm, 21.4 μm, 18.5 μm, and 16.3 μm, respectively. The average grain sizes were smaller than that of pure BCT ceramic, indicating the inhibition effect on grain growth of BST [14]. The decrease in grain size could be related to the solute resistance mechanism. The change in ionic radius between the dopant and the body leads to the lattice strain energy (ΔG_{strain}), which can be expressed by the following Eq. (1) [23]:

$$\Delta G_{strain} = 4\pi M N_A \left[\frac{r_0}{2(r_d - r_0)^2} + \frac{1}{3}(r_d - r_0)^3 \right] \quad (1)$$

where r_0, r_d, N_A, and M represent the optimal radius of the lattice site, the ionic radius of the dopant, Avogadro's constant, and Young's modulus, respec-
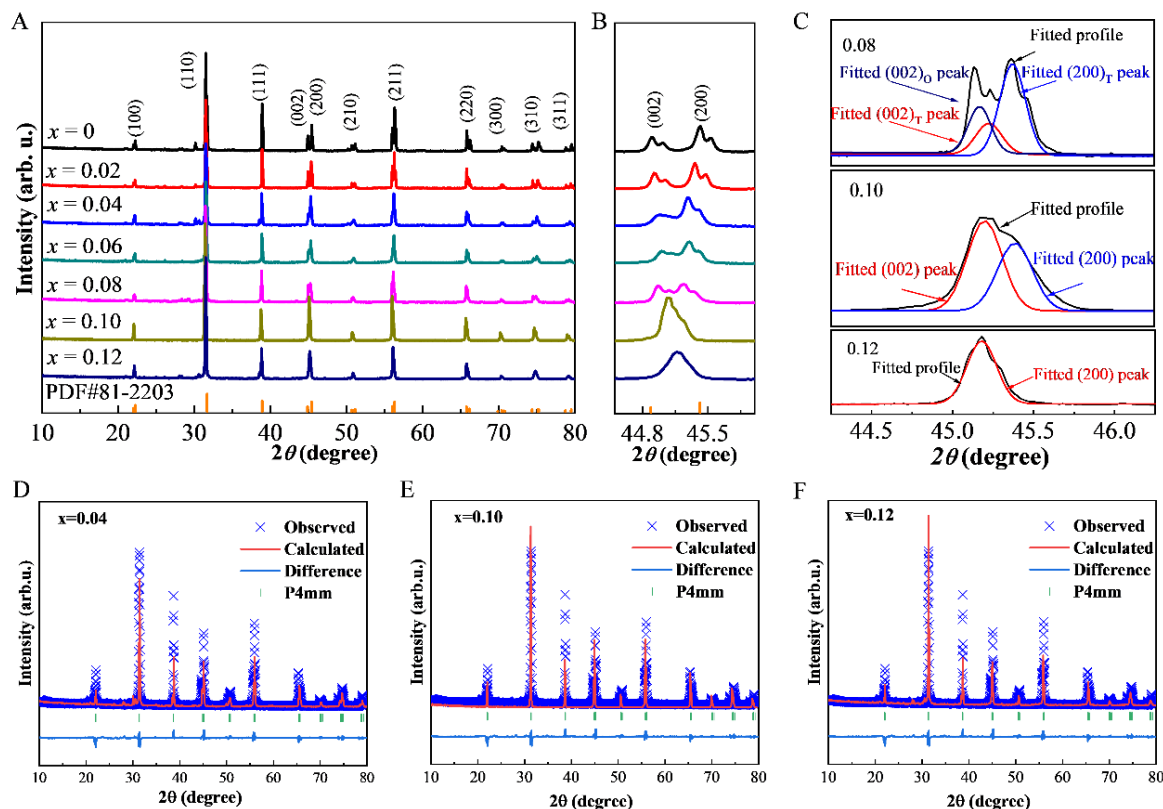
Fig. 1 (A) XRD patterns of the (1-x)BCT-xBST ($0 \leqslant x \leqslant 0.12$) ceramics; (B) XRD patterns of the samples in the range of 2θ from $44°$ to $46°$; (C) diffraction peaks fitting of the (200) diffraction reflection for the samples with x = 0.04–0.12; (D–F) XRD Rietveld refinement results of (D) x = 0.04, (E) x = 0.10 and (F) x = 0.12.
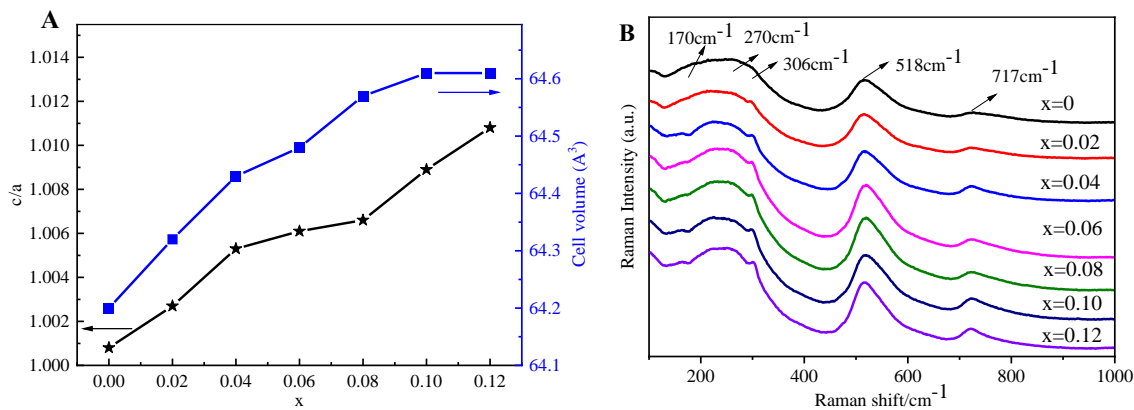

Fig. 2 (A) Cell parameters and cell volume of the (1-x)BCT-xBST ($0 \leqslant x \leqslant 0.12$) ceramics; (B) room temperature Raman spectra of the (1-x)BCT-xBST ($0 \leqslant x \leqslant 0.12$) ceramics.

tively. Occupation of Ti^{4+} (0.605 Å) sites by larger Sn^{4+} (0.69 Å) led to an increase in ΔG_{strain}, which hindered grain boundary migration and inhibited grain growth. The average grain size and relative density of all the ceramics were further demonstrated in Fig. 4H, and comprehensively demonstrated in Fig. 5H. The

corresponding relative densities of the samples increased from 91% (x = 0) to a peak value of 97.3% (x = 0.10), before experiencing a slight decrease to 93.6% at x = 0.12. This densification process was crucial in the ceramics as it significantly enhanced the breakdown strength [12]. The improved densification
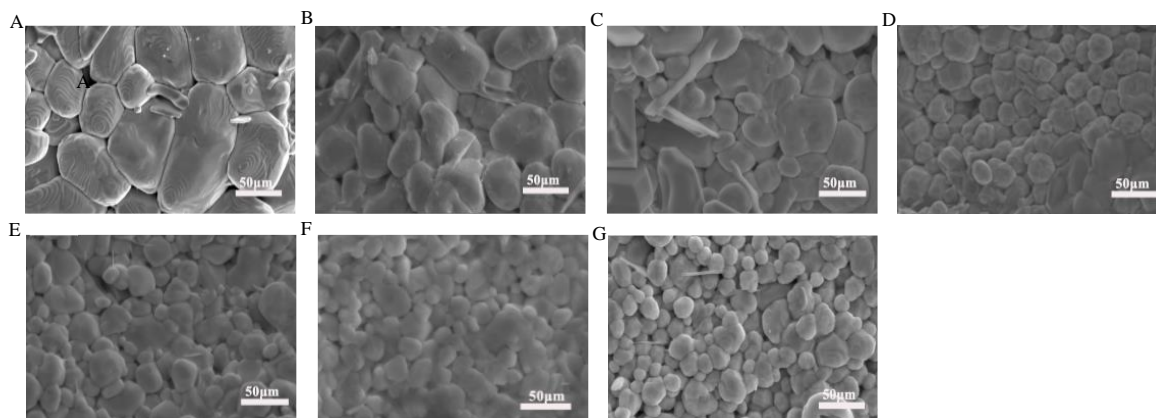
Fig. 3 SEM image of the (1-x)BCT-xBST ceramics at different values of x (0–0.12). A, x = 0; B, x = 0.02; C, x = 0.04; D, x = 0.06; E, x = 0.08; F, x = 0.10; G, x = 0.12.
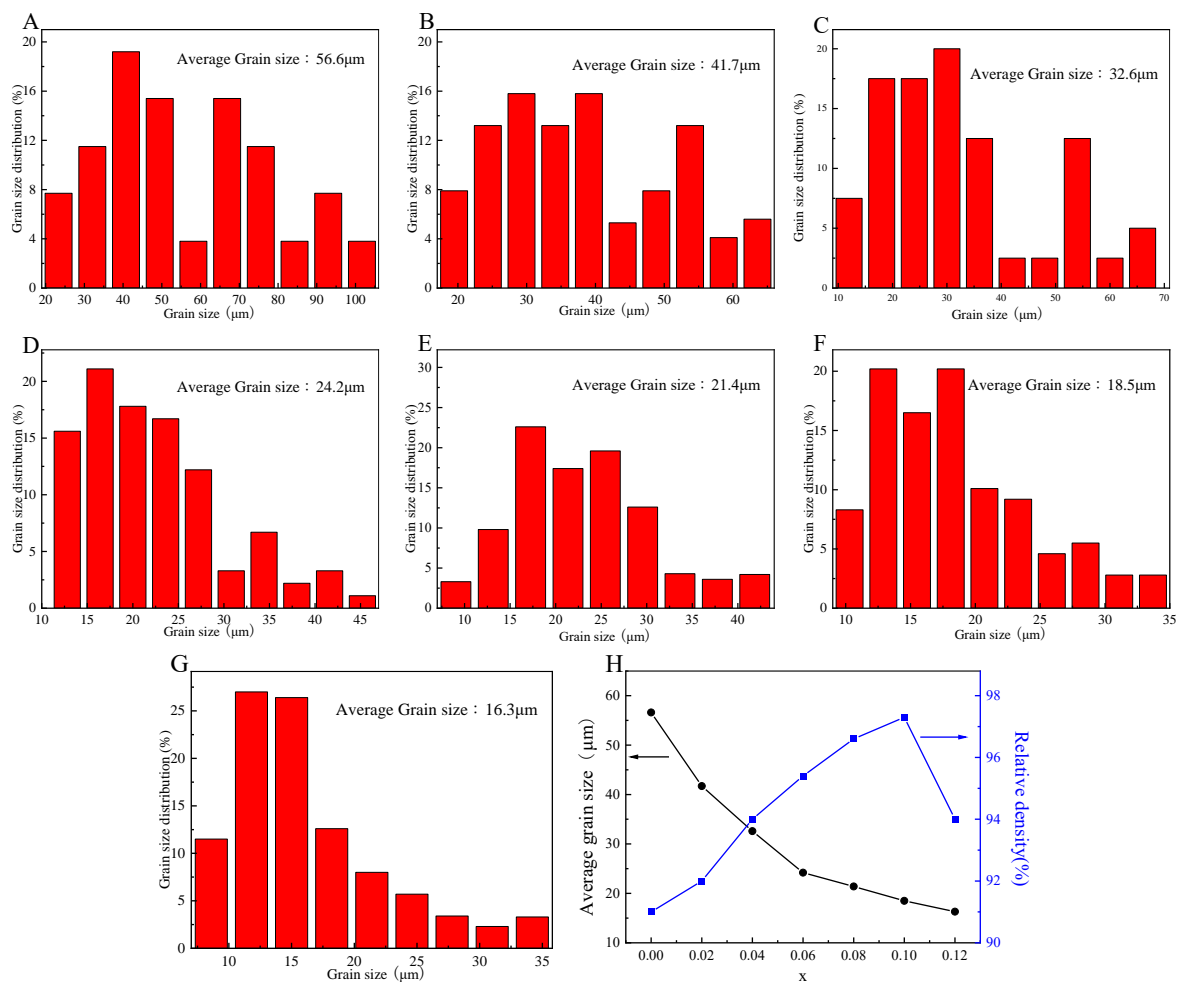

Fig. 4 (A–G) Grain size distribution and average grain size of different compositions; (H) variations in grain size and relative density of all the ceramics.
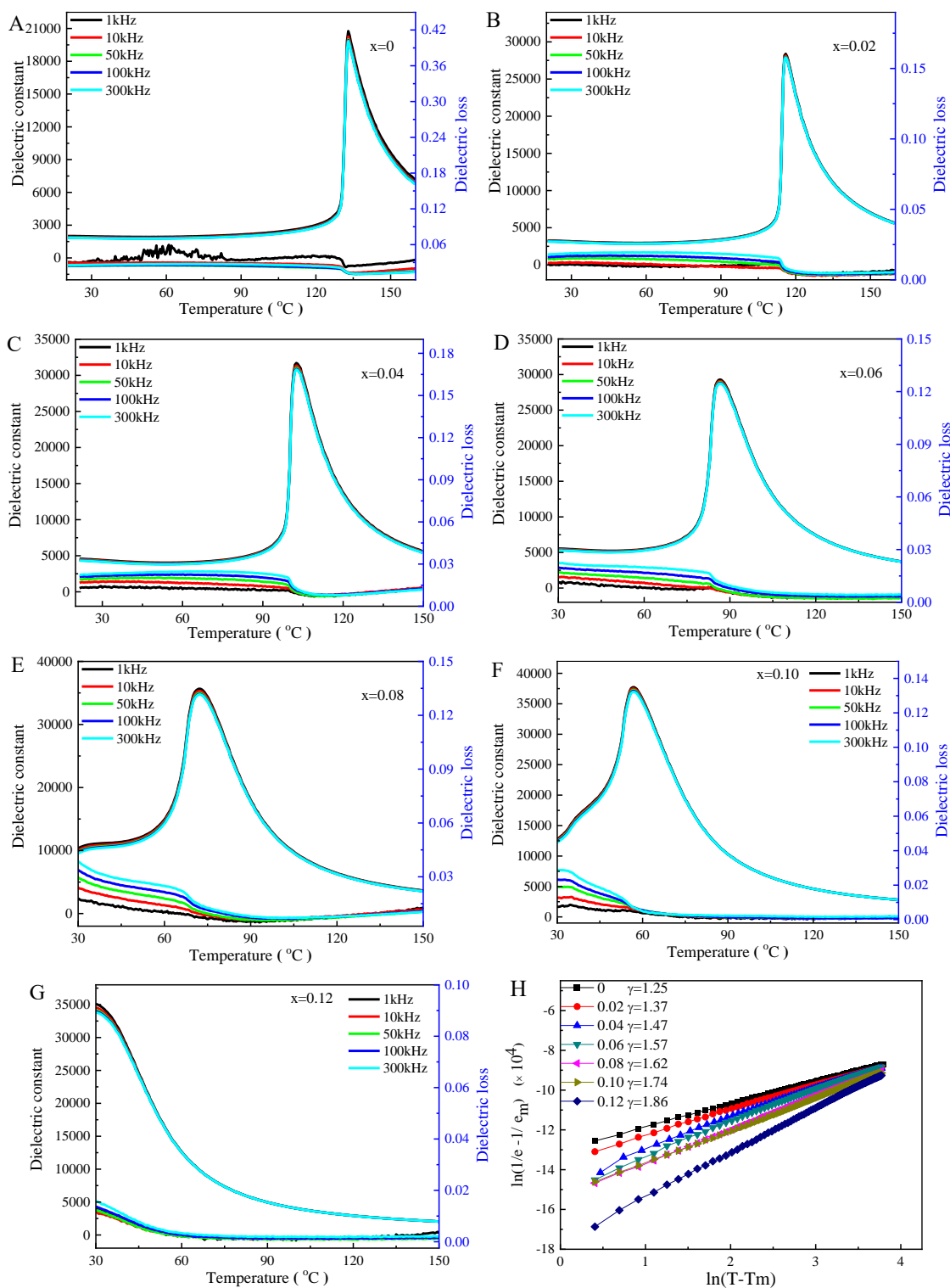
Fig. 5 (A–H) Temperature dependence of dielectric constant and dielectric loss of the (1-x)BCT-xBST ceramics with x = 0–0.12 at different frequencies; (I) $\ln(1/\varepsilon - 1/\varepsilon_m)$ vs. $\ln(T - T_m)$ plot for the (1-x)BCT-xBST (x = 0–0.12) ceramics at 1 kHz.
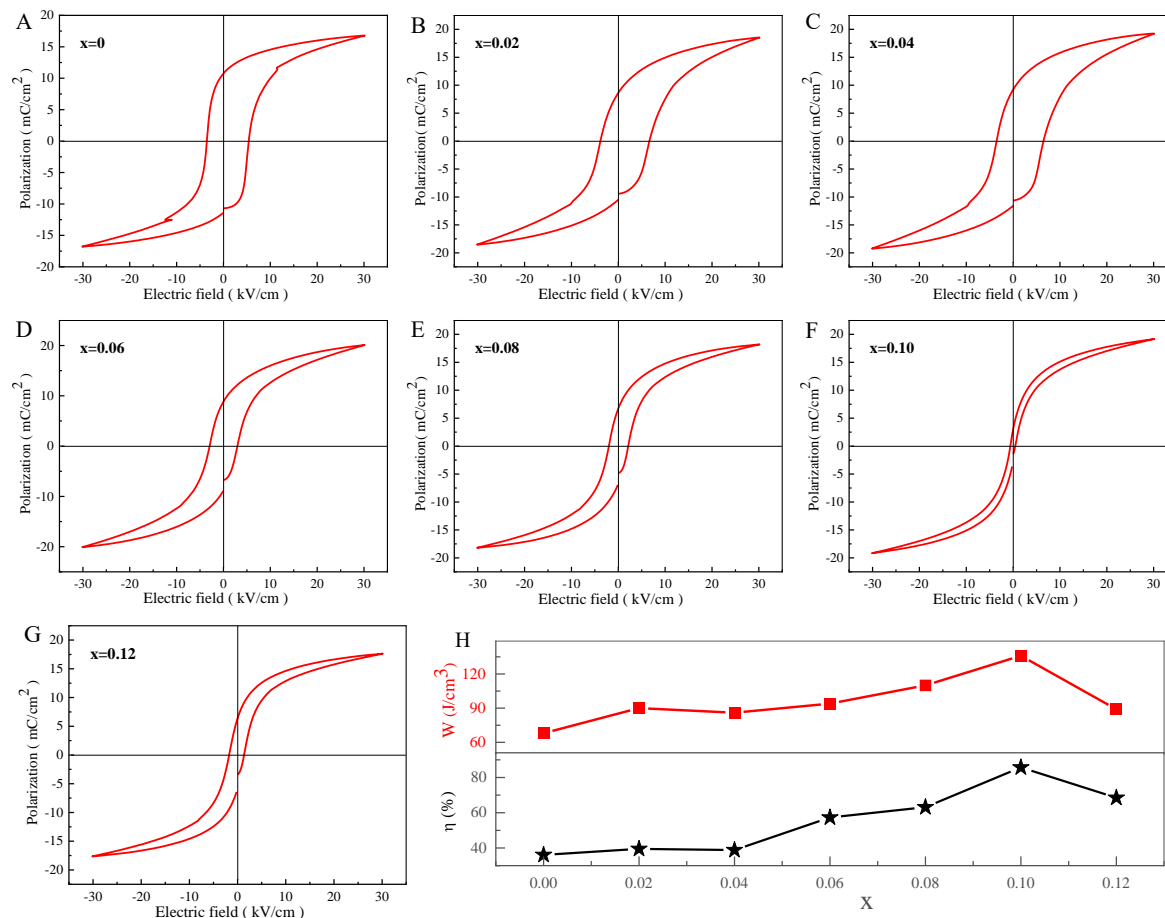
Fig. 6 (A–G) Electric field (P-E) hysteresis loops of the (1-x)BCT-xBST (x = 0–0.12) ceramics at the electric field of 30 kV/cm (10 Hz) at room temperature; (H) graphs of the energy storage density (W) and the energy storage efficiency (η) as a function of BST.

Table 1 Rietveld refinement fitting results and lattice parameter of each component.

Sample	O phase (%)	T phase (%)	χ^2	R_{wp}	R_p
x = 0	83.11	16.89	3.45	8.14	6.33
x = 0.02	72.15	27.85	5.81	5.36	4.79
x = 0.04	60.39	39.61	6.17	6.75	5.42
x = 0.06	47.21	52.79	5.17	7.14	5.29
x = 0.08	32.46	67.54	4.19	6.28	6.37
x = 0.10	18.44	81.56	6.31	5.97	4.26
x = 0.12	7.44	92.56	3.34	6.71	3.96

Table 2 Comparison of energy storage properties of the (1-x)BCT-xBST ceramics and other lead-free ceramics (W, energy storage density; η, energy storage efficiency; E, applied electric field).

Composition	W (mJ/cm^3)	η (%)	E (kV/cm)	Ref.
BCT-BST	138	87.51%	30	This work
BCZT	246	50%	40	[33]
0.88BT-0.12BLN	210	60%	40	[34]
BZT	162	65%	40	[35]
BLTZS	65	60	12	[36]
BT-BBP	69	72.58%	15	[37]
BCT-BZT	164	74%	40	[38]
SBTS	121	77%	40	[39]
ST-NBT-BT	60	77.06%	20	[40]

not only bolstered the mechanical robustness but also augmented the electrical insulation properties, making these ceramics highly suited for a variety of high-performance industrial applications. The decrease in relative density at x = 0.12 could be resulted from exceeding the BST solubility in $BaTiO_3$, leading to incomplete integration and potential secondary phase formation, and subsequently impaired the density. Increased BST content could also disrupt pore distribution, create voids during sintering, and hence reduce the density.

The temperature dependence of dielectric constant and dielectric loss of the (1-x)BCT-xBST ceramics with x = 0–0.12 at different frequencies from 1 kHz to 300 kHz were presented in Fig. 5A–H. The dielectric constant of samples showed a single dielectric peak, and decreased roughly with the increasing of frequency, revealing the frequency dispersion characteristic. These results were attributed to the dipole keeping up with the frequency of the field [24]. The frequency characteristics were also observed in dielectric loss, which was considered to be the sign of ferroelectrics relaxation [25]. Curie temperature decreased linearly with increasing x values at the same frequency, indicating the transition from paraelectric phase to ferroelectric phase. The results were similar to the situations reported in the literature [26]. The dielectric constant experienced a significant enhancement and reached its peak value when x equaled 0.10 at the same frequency. This enhancement was primarily attributed to the reduction in the width of the 90° domain walls within the (1-x)BCT-xBST ceramics [22]. The narrower domain walls facilitated greater mobility under an applied electric field, thereby amplifying the materials dielectric response. However, as x continued to increase beyond 0.10, the dielectric constant began to decline, largely due to the rising volume fraction of grain boundaries within the ceramic matrix [26]. The increase of grain boundaries hindered the movement of domain walls, which in turn diminished the overall dielectric response. This interplay between domain wall dynamics and grain boundary underscored the complex nature of the dielectric behavior in these materials, highlighting the critical role of microstructural features in determining macroscopic properties [27, 28]. The dielectric loss of ceramics decreased with increasing x values, revealing the ceramics' possession of excellent dielectric breakdown strength (DBS) for energy storage at low electric field.

The relaxation behavior of the (1-x)BCT-xBST (x = 0–0.12) ceramics with different compositions above Curie temperature T_c can be expressed by the modified Curie-Weiss law in Eq. (2) [29]:

$$\frac{1}{\varepsilon} - \frac{1}{\varepsilon_m} = \frac{(T - T_m)^\gamma}{C} \tag{2}$$

where ε, ε_m, T, T_m, C, and γ represent the dielectric

constant, the maximum dielectric constant, temperature, the temperature of ε_m, Curie constant, and diffusion factor, respectively. According to the law, the values of diffusion parameter γ were between 1, for normal ferroelectric, and 2, for idea relax or ferroelectric. The curve plotted between $\ln(1/\varepsilon - 1/\varepsilon_m)$ and $\ln(T - T_m)$ was demonstrated in Fig. 5I. The γ values were 1.25, 1.37, 1.47, 1.57, 1.62, 1.74, and 1.86 for the samples of x = 0, 0.02, 0.04, 0.06, 0.08, 0.10, and 0.12, respectively. These results indicated that the relaxation behavior of the ceramics could be strengthened by incorporation of Sn.

Fig. 6A–G shows well-saturated hysteresis loops (P-E) curves of (1-x)BCT-xBST (x = 0–0.12) ceramics at room temperature at 30 kV/cm. The thinness of the P-E loops increased with x, indicating that the uniform and dense microstructure would reduce the irreversibility of the electric dipoles in the crystal, resulting in the pinching effect under the external electric field [27]. With the increase of x, the maximum polarization (Pmax) value of the sample increased from 16.8 $\mu C/cm^2$ (for x = 0) to 20.4 $\mu C/cm^2$ (for x = 0.10), attributed to the split of long-range ordered ferroelectric domains into many small nano-domains, resulting in an increase of rapid turning and migration of the electric domains under the external electric field. However, when the BST content increased to x = 0.12, the P_{max} value reduced to 17.63 $\mu C/cm^2$. According to the Maxwell-Wagner (MW) mechanism of grain boundaries [30, 31], the number of dipoles in the unit cell decreased during the T and O phase transition, which was not conducive to local electric field formation, thus reducing P_{max}.

Fig. 6H shows the energy storage density (W) and the energy storage efficiency (η) as a function of BST. In general, the energy storage characteristics of dielectric capacitors could be determined from the corresponding polarization-dependent electric field relationship curves (P-E), following correlation Eqs. (3)–(5) [32]:

$$W_{\text{total}} = \int_0^{P_{\max}} E \, dP \tag{3}$$

$$W_{\text{rec}} = \int_{P_r}^{P_{\max}} E \, dP \tag{4}$$

$$\eta = \frac{W_{\text{rec}}}{W_{\text{total}}} \times 100\% \tag{5}$$

where $P_{\max}$ and P_r represent the maximum and the residual polarization strengths, respectively; and E represents the applied electric field. According to Eq. (4), the energy storage densities and efficiencies of the components of the BTC-BST ceramics were obtained. Fig. 6H shows that the W_{rec} and the η values of the samples had a similar trend, gradually increasing from 71 mJ/cm^3 and 37.21% (x = 0) to the maximum values of 128 mJ/cm^3 and 87.51% (x =

0.10). The result was attributed to the introduction of BST causing the reorientation of the dipoles inside the lattice and the obtainment of the short-range ordered ferroelectric domains and, thus, improving the energy storage performance. With further increase of x, the sample coexisting with T and O phases was gradually transformed into dominated T phase, contributing to a decrease in the number of dipoles in the lattice of the sample and a gradual decrease in the rotational energy barrier of polarization and resulting in a decrease in the storage density and efficiency to 91 mJ/cm^3 and 68.49% (x = 0.12), respectively.

The formation of MPB at room temperature lowered the energy barrier for polarization rotation, improving the energy storage properties. The decrease in the energy storage density and the energy storage efficiency could be attributed to phase transition [41]. A comparison of the energy storage density and the efficiency and electric field (E) achieved in this work with those of other lead-free ceramics were listed in Table 2, illustrating excellent energy storage properties of the (1-x)BCT-xBST ceramics at low electric field.

CONCLUSION

The (1-x)Ba$_{0.9}$Ca$_{0.1}$TiO$_3$-xBaSn$_{0.1}$Ti$_{0.9}$O$_3$ (x = 0–0.12) lead-free ceramics were fabricated by traditional solid-state method. All the samples presented a single perovskite-type structure, and the average grain size of ceramics decreased with the addition of BST. It was worth noting that the (1-x)BCT-xBST ceramics exhibited a high dielectric constant, low dielectric loss, large recoverable energy density (W = 138 mJ/cm^3), and excellent energy storage efficiency (η = 87.51%) at low electric field of 30 kV/cm at x = 0.10, indicating a promising prospect of the (1-x)BCT-xBST ceramics in energy storage application in low field region.

REFERENCES

1. Jaita P, Jarupoom P (2020) Temperature dependence on structure, mechanical and electrical properties of bismuth lanthanum sodium titanate-modified lead zirconate titanate ceramics. *ScienceAsia* **46S**, 51–57.
2. Pan H, Lan S, Xu S, Zhang Q, Yao H, Liu Y, Meng F, Guo EJ, et al (2021) Ultrahigh energy storage in superparaelectric relaxor ferroelectrics. *Science* **374**, 100–104.
3. Li X, Chen X, Sun J, Zhou M, Zhou H (2020) Novel lead-free ceramic capacitors with high energy density and fast discharge performance. *Ceram Int* **46**, 3426–3432.
4. Saenkam K, Jaita P, Sirisoonthorn S, Tunkasiri T, Rujijangul G (2021) Effects of processing parameter on energy storage density and ferroelectric properties of lead-free bismuth sodium titanate-strontium bismuth titanate ceramics. *ScienceAsia* **47S**, 34–41.
5. Fan Y, Zhou Z, Chen Y, Huang W, Dong X (2020) A novel lead-free and high-performance barium strontium titanate-based thin film capacitor with ultrahigh energy storage density and giant power density. *J Mater Chem C* **8**, 50–57.
6. Xu B, Íñiguez J, Bellaiche L (2017) Designing lead-free antiferroelectrics for energy storage. *Nat Commun* **8**, 15682.
7. Tang Y, Zhao Z, Hao X, Wang Y, Liu Y, Hou Y, Yang Q, et al (2017) Engineering hollow polyhedrons structured from carbon-coated CoSe$_2$ nanospheres bridged by CNTs with boosted sodium storage performance. *J Mater Chem A* **5**, 13591–13600.
8. Li W, Wu S, Zhang H, Zhang X, Zhuang J, Hu C, Liu Y, Lei B, et al (2018) Enhanced biological photosynthetic efficiency using light-harvesting engineering with dual-emissive carbon dots. *Adv Funct Materials* **28**, 1804004.
9. Jayakrishnan AR, Alex KV, Thomas A, Silva JPB, Kamakshi K, Dabra N, Sekhar KC, Agostinho Moreira J, et al (2019) Composition-dependent xBa(Zr$_{0.2}$Ti$_{0.8}$)O$_3$-(1-x)(Ba$_{0.7}$Ca$_{0.3}$)TiO$_3$ bulk ceramics for high energy storage applications. *Ceram Int* **45**, 5808–5818.
10. Zhu L-F, Zhang B-P, Zhao L, Li S, Zhou Y, Shi X-C, Wang N (2016) Large piezoelectric effect of (Ba,Ca)TiO$_3$-xBa(Sn,Ti)O$_3$ lead-free ceramics. *J Eur Ceram Soc* **36**, 1017–1024.
11. Yu S, Zhang C, Wu M, Dong H, Li L (2019) Ultra-high energy density thin-film capacitors with high power density using BaSn$_{0.15}$Ti$_{0.85}$O$_3$/Ba$_{0.6}$Sr$_{0.4}$TiO$_3$ heterostructure thin films. *J Power Sources* **412**, 648–654.
12. Puli VS, Pradhan DK, Riggs BC, Adireddy S, Katiyar RS, Chrisey DB (2014) Synthesis and characterization of lead-free ternary component BST-BCT-BZT ceramic capacitors. *J Adv Dielect* **4**, 1450014.
13. Liu G, Li Y, Gao J, Li D, Yu L, Dong J, Zhang Y, Yan Y, et al (2020) Structure evolution, ferroelectric properties, and energy storage performance of CaSnO$_3$ modified BaTiO$_3$-based Pb-free ceramics. *J Alloys Compd* **826**, 154160.
14. Zhang L, Pu Y, Chen M, Li R, Guo X, Cui Y (2018) Enhanced energy-storage properties of (1-x)Na$_{0.5}$Bi$_{0.5}$TiO$_3$-xBaSnO$_3$ ceramics. *Ceram Int* **44**, S207–210.
15. Shi P, Zhu L, Gao W, Yu Z, Lou X, Wang X, Yang Z, Yang S (2019) Large energy storage properties of lead-free (1-x)(0.72Bi$_{0.5}$Na$_{0.5}$TiO$_3$-0.28SrTiO$_3$)-xBiAlO$_3$ ceramics at broad temperature range. *J Alloys Compd* **784**, 788–793.
16. Jiang X, Hao H, Zhang S, Lv J, Cao M, Yao Z, Liu H (2019) Enhanced energy storage and fast discharge properties of BaTiO$_3$ based ceramics modified by Bi(Mg$_{1/2}$Zr$_{1/2}$)O$_3$. *J Eur Ceram Soc* **39**, 1103–1109.
17. Wang H, Liu J, Zhai J, Shen B, Pan Z, Liu JR, Yang K (2017) Effect of crystallization temperature on dielectric and energy-storage properties in SrO-Na$_2$O-Nb$_2$O$_5$-SiO$_2$ glass-ceramics. *Ceram Int* **43**, 8898–8904.
18. Ding S-Y, Yi J, Li J-F, Ren B, Wu D-Y, Panneerselvam R, Tian Z-Q (2016) Nanostructure-based plasmon-enhanced Raman spectroscopy for surface analysis of materials. *Nat Rev Mater* **1**, 16021.
19. Swain AB, Subramanian V, Murugavel P (2018) The role of precursors on piezoelectric and ferroelectric characteristics of 0.5BCT-0.5BZT ceramic. *Ceram Int* **44**, 6861–6865.
20. Gao J, Liu Y, Wang Y, Wang D, Zhong L,

Ren X (2017) High temperature-stability of $(Pb_{0.9}La_{0.1})(Zr_{0.65}Ti_{0.35})O_3$ ceramic for energy-storage applications at finite electric field strength. *Scripta Mater* **137**, 114–118.

21. Strathdee T, Luisman L, Feteira A, Reichmann K (2011) Ferroelectric-to-relaxor crossover in $(1-x)BaTiO_3$-$xBiYbO_3$ ($0 \leqslant x \leqslant 0.08$) ceramics. *J Am Ceram Soc* **94**, 2292–2295.

22. Guo S, Luo B, Xing H, Wang J, Zeeshan HM, Jin K, Chen C (2020) Ferroelectric, dielectric, and impedance properties of Sm-modified $Ba(Zr_{0.2}Ti_{0.8})O_3$-$x(Ba_{0.7}Ca_{0.3})TiO_3$ ceramics. *Ceram Inter* **46**, 7198–7203.

23. Wang Y, Pu Y, Li X, Zheng H (2016) Structural evolution, relaxation behaviors and dielectric properties of $BaTiO_3$-$BiAlO_3$ perovskite solid solutions. *J Mater Sci Mater Electron* **27**, 11565–11571.

24. Schileo G, Luisman L, Feteira A, Deluca M, Reichmann K (2013) Structure-property relationships in $BaTiO_3$-$BiFeO_3$-$BiYbO_3$ ceramics. *J Eur Ceram Soc* **33**, 1457–1468.

25. Jain A, Wang YG, Wang N, Wang FL (2020) Critical role of CuO doping on energy storage performance and electromechanical properties of $Ba_{0.8}Sr_{0.1}Ca_{0.1}Ti_{0.9}Zr_{0.1}O_3$ ceramics. *Ceram Inter* **46**, 18800–18812.

26. Abdessalem MB, Aydi S, Aydi A, Abdelmoula N, Sassi Z, Khemakhem H (2017) Polymorphic phase transition and morphotropic phase boundary in $Ba_{1-x}Ca_xTi_{1-y}Zry$ O_3 ceramics. *Appl Phys A* **123**, 583.

27. Xie J, Hao H, Liu H, Yao Z, Song Z, Zhang L, Xu Q, Dai J, Cao M (2016) Dielectric relaxation behavior and energy storage properties of Sn modified $SrTiO_3$ based ceramics. *Ceram Inter* **42**, 12796–12801.

28. Jain A, Wang YG, Guo H (2020) Microstructural properties and ultrahigh energy storage density in $Ba_{0.9}Ca_{0.1}TiO_3$-$NaNb_{0.85}Ta_{0.15}O_3$ relaxor ceramics. *Ceram Inter* **46**, 24333–233446.

29. Liu J, Ren K, Ma C, Du H, Wang Y (2000) Dielectric and energy storage properties of flash-sintered high-entropy $(Bi_{0.2}Na_{0.2}K_{0.2}Ba_{0.2}Ca_{0.2})TiO_3$ ceramic. *Ceram Inter* 2020, **46**, 20576–20581.

30. Li Z, Bian Z, Ren Y, Chen Z, Xu J (2024) Enhanced energy storage performance in $Na(Nb,Ta)O_3$-doped $Ba(Ti,Ca)O_3$-based ceramics through bidirectional optimization strategy. *Mater Res Bull* **173**, 112664.

31. Wada S, Yano M, Suzuki T, Noma T (2000) Crystal structure of barium titanate fine particles including Mg and analysis of their lattice vibration. *J Mater Sci* **35**, 3889–3902.

32. Li Z, Chen Z, Xu J (2022) Enhanced energy storage performance of $BaTi_{0.97}Ca_{0.03}O_{2.97}$-based ceramics by doping high-entropy perovskite oxide. *J Alloys Compd* **922**, 166179.

33. Jain A, Wang YG, Wang N, Li Y, Wang FL (2020) Tuning the dielectric, ferroelectric and electromechanical properties of $Ba_{0.83}Ca_{0.10}Sr_{0.07}TiO_3$-$MnFe_2O_4$ multiferroic composites. *Ceram Inter* **46**, 7576–7585.

34. Jain A, Wang YG, Shi LN (2022) Recent developments in $BaTiO_3$ based lead-free materials for energy storage applications. *J Alloys Compd* **928**, 167066.

35. Ma C, Tan X (2010) Morphotropic phase boundary and electrical properties of lead-free $(1-x)BaTiO_3$-$xBi(Li_{1/3}Ti_{2/3})O_3$ ceramics. *J Appl Phys* **107**, 124108.

36. Kushvaha DK, Rout SK, Tiwari B (2020) Density dependent ionic transport in polycrystalline $SrNb_2O_6$ ceramic. *Physica B Condensed Matter* **579**, 411910.

37. Li W-B, Zhou D, Pang L-X, Xu R, Guo H-H (2017) Novel barium titanate based capacitors with high energy density and fast discharge performance. *J Mater Chem A* **5**, 19607–19612.

38. Badapanda T, Chaterjee S, Mishra A, Ranjan R, Anwar S (2017) Electric field induced strain, switching and energy storage behaviour of lead free barium zirconium titanate ceramic. *Physica B Condensed Matter* **521**, 264–269.

39. Smail S, Benyoussef M, Taïbi K, Bensemma N, Manoun B, El Marssi M, Lahmar A (2020) Structural, dielectric, electrocaloric and energy storage properties of lead free $Ba_{0.975}La_{0.017}(Zr_xTi_{0.95-x})Sn_{0.05}O_3$ ($x = 0.05$; 0.20) ceramics. *Mater Chem Phys* **252**, 123462.

40. Haily E, Bih L, El Bouari A, Lahmar A, Elmarssi M, Manoun B (2020) Effect of BaO-Bi_2O_3-P_2O_5 glass additive on structural, dielectric and energy storage properties of $BaTiO_3$ ceramics. *Mater Chem Phys* **241**, 122434.

41. Luo Q, Ma H, Hou Q, Li Y, Ren J, Dai X, Yao Z, Zhou Y, et al (2018) All-carbon-electrode-based endurable flexible perovskite solar cells. *Adv Funct Mater* **28**, 1706777.

42. Cui C, Pu Y, Shi R (2018) High-energy storage performance in lead-free $(0.8-x)SrTiO_3$-$0.2Na_{0.5}Bi_{0.5}TiO_3$-$xBaTiO_3$ relaxor ferroelectric ceramics. *J Alloys Compd* **740**, 1180–1187.